Flavor conversions with energy-dependent neutrino emission and absorption

Chinami Kato*
Faculty of Science and Technology, Tokyo University of Science, 2641 Yamazaki, Noda-shi, Chiba 278-8510, Japan

Hiroki Nagakura
National Astronomical Observatory of Japan, 2-21-1 Osawa, Mitaka, Tokyo 181-8588, Japan

Masamichi Zaizen
Faculty of Science and Engineering, Waseda University, Tokyo 169-8555, Japan

(Received 3 April 2023; accepted 17 May 2023; published 5 July 2023)

Fast neutrino flavor conversions (FFCs) and collisional flavor instabilities (CFIs) potentially affect the dynamics of core-collapse supernovae and binary neutron star mergers. Under the assumption of homogeneous neutrinos, we investigate effects of neutrino emission and absorption (EA) by matter through both single and multienergy numerical simulations with a physically motivated setup. In our models, FFCs dominate over CFIs in the early phase, while EA secularly and significantly have impact on flavor conversions. They facilitate angular swaps or the full exchange between electron neutrinos (ν_e) and heavy-leptonic neutrinos (ν_x). As a result, the number density of ν_x becomes more abundant than the case without EA, despite the fact that the isotropization by EA terminates the FFCs earlier. In the later phase, the system approaches new asymptotic states characterized by EA and CFIs, in which rich energy-dependent structures also emerge. Multienergy effects sustain FFCs and the time evolution of the flavor conversion becomes energy dependent, which are essentially in line with effects of the isoenergetic scattering that we have studied previously. We also find that ν_x in the high-energy region convert into ν_e via flavor conversions and then they are absorbed through charged-current reactions, exhibiting the possibility of new path of heating matter.

DOI: 10.1103/PhysRevD.108.023006

I. INTRODUCTION

Decades of theoretical research on core-collapse supernovae (CCSNe) and binary neutron star mergers (BNSMs) have shown that neutrinos play important roles in the dynamics of these explosive transient events. The influence of neutrino physics in these phenomena has been much discussed. One of the quantum kinetic features receiving increased attention throughout the community is collective neutrino oscillations, which are neutrino flavor conversions induced by neutrino self-interactions [1–4]. Fast neutrino flavor conversions (FFCs) [4] and collisional flavor instabilities (CFIs) [5] potentially affect the dynamics. The sensitivity of CCSN and BNSM dynamics to these flavor conversions have been recently discussed [6–10], although there is very little known about their nonlinear properties.

FFC can occur independent of vacuum oscillations and its dynamics is essentially energy independent. It has been found that electron neutrino lepton number crossings (ELN crossings) in angular distributions are a necessary and sufficient condition for FFCs [11,12]. The associated criterion, namely, ELN-XLN crossing, also offers to determine asymptotic states of FFCs in the nonlinear regime [13,14], where XLN denotes a heavy-leptonic neutrino lepton number. Recent studies have found that the ELN crossings are ubiquitous in CCSNe [15–31] and BNSMs [6,7,32–37]. This suggests that we need to accommodate FFCs in the theoretical modeling of CCSNe and BNSMs.

Nonlinear dynamics of FFCs have been simulated by solving the neutrino quantum kinetic equation (QKE) [7,37–47]. Under the assumption of homogeneous neutrinos, the dynamics can be described in analogy with pendulum motions [48,49]. Although the pendulum analogy offers deeper insights into FFCs, this toy model cannot be applied in the case with neutrino-matter collisions [50,51]; indeed, the FFC dynamics becomes qualitatively different [50,52–58]. Recent studies also performed large-scale simulations of FFCs with collisions at various levels of approximations [8,9,13,59–61]. We refer readers to [62–64] for recent reviews.

*ckato@rs.tus.ac.jp

As mentioned above, matter collisions potentially have a significant impact on the dynamics of flavor conversions. CFI, which is a flavor conversion induced by matter collisions, has recently attracted much attention [5]. One of the necessary conditions for CFIs is the difference of reaction rates between neutrinos and antineutrinos [65]. A notable feature of CFIs is that flavor conversions occur even for isotropic neutrino distributions [5]. Some recent studies suggested that CFIs can ubiquitously occur in CCSN [8] and BNSM [65] environments. It is also noteworthy that the growth rate of CFIs has a resonant structure, if the number density of electron neutrinos (ν_e) and their antipartners $\bar{\nu}_e$ is nearly equal to each other [65,66]. If FFCs are parasitically induced by CFIs, the flavor conversions may be further accelerated [67].

One thing we do notice is that the nonlinear interplay between flavor conversions and matter collisions remains an open question, even in the case of homogeneous neutrino assumption. As for FFCs, the coupling with isoenergetic scattering such as nucleon scattering has been studied [50,55–57], whereas the impact of emission and absorption on flavor conversions has not yet been investigated in detail. It should also be mentioned that, although the interplay between CFIs and emission/absorption has been already investigated [5,65–68], there have been little study on the cases with anisotropic distributions or nonmonochromatic neutrinos [65,67]. A better understanding of roles of emission/absorption on these flavor conversions can contribute valuable information to interpret results obtained from more self-consistent and global simulations of FFCs and CFIs [8,9], and it may also offer new quantum kinetic features of neutrinos.

In this paper, we perform single and multienergy dynamical simulations of flavor evolution with neutrino emission and absorption. Neutrinos are assumed to be homogeneous space and axial symmetric (but anisotropic) in momentum space. It is also assumed that the system consists of two-neutrino flavors. In this study, we pay particular attention to the energy- and angular-dependent features of flavor conversions. One of the intriguing features found in this study is that the so-called angular swap, which corresponds to the full exchange between ν_e and heavy-leptonic neutrinos (ν_x) at a certain angular region, is facilitated by emission and absorption. We will discuss the possible generation mechanism.

This paper is organized as follows. We start with the numerical setup for dynamical simulations of flavor conversions in Sec. II. We then move on to investigate effects of neutrino emission and absorption on flavor conversions with the energy-independent reaction rates from various perspectives in Sec. III. In Sec. IV, we extend the study to the case of energy-dependent emission and absorption. Finally, we summarize our key findings and conclusions in Sec. V.

II. NUMERICAL SETUP

Time evolution of neutrinos in phase space follows the QKEs [2,69],

$$i\left(\frac{\partial}{\partial t}+\vec{v}\cdot\nabla\right)\rho(\vec{x},\vec{p},t)=[\mathcal{H},\rho(\vec{x},\vec{p},t)]+i\mathcal{C}[\rho], \quad (1)$$

$$i\left(\frac{\partial}{\partial t}+\vec{v}\cdot\nabla\right)\bar{\rho}(\vec{x},\vec{p},t)=[\bar{\mathcal{H}},\bar{\rho}(\vec{x},\vec{p},t)]+i\bar{\mathcal{C}}[\bar{\rho}]. \quad (2)$$

In these expressions, ρ is the density matrix for neutrinos, $\mathcal{H}$ is the Hamiltonian potential, and C is the collision term. The bar description indicates the quantities for antineutrinos hereafter. We consider a two flavor system composed of electron and heavy-leptonic neutrinos. Accordingly, ρ and $\bar{\rho}$ have four components,

$$\rho=\begin{pmatrix}\rho_{ee} & \rho_{ex}\\ \rho_{ex}^* & \rho_{xx}\end{pmatrix}, \qquad \bar{\rho}=\begin{pmatrix}\bar{\rho}_{ee} & \bar{\rho}_{ex}\\ \bar{\rho}_{ex}^* & \bar{\rho}_{xx}\end{pmatrix}. \quad (3)$$

It is also assumed that the neutrino distribution is spatially homogeneous and axial symmetric in momentum space. In this study, we include neutrino emission and absorption via charged-current interactions with surrounding matter. Since heavy leptons are unlikely to appear in CCSNe and BNSMs (but see Ref. [70]), we ignore the charged-current reactions for ν_x and their antipartners ($\bar{\nu}_x$).

Under these assumptions, the QKEs can be rewritten as

$$i\frac{\partial\rho_a}{\partial t}=[\mathcal{H}_{\nu\nu},\rho_a]+i\begin{pmatrix}2\pi R_e-[R_e+R_a]\rho_{ee,a} & -\frac{1}{2}[R_e+R_a]\rho_{ex,a}\\ -\frac{1}{2}[R_e+R_a]\rho_{xe,a} & 0\end{pmatrix}, \quad (4)$$

$$i\frac{\partial\bar{\rho}_a}{\partial t}=[\bar{\mathcal{H}}_{\nu\nu},\bar{\rho}_a]+i\begin{pmatrix}2\pi\bar{R}_e-[\bar{R}_e+\bar{R}_a]\bar{\rho}_{ee,a} & -\frac{1}{2}[\bar{R}_e+\bar{R}_a]\bar{\rho}_{ex,a}\\ -\frac{1}{2}[\bar{R}_e+\bar{R}_a]\bar{\rho}_{xe,a} & 0\end{pmatrix}, \quad (5)$$

with the azimuthal-angle-integrated density matrix $\rho_a\equiv\rho_a(E_\nu,\cos\theta_\nu,t)=\int d\phi_\nu\rho(E_\nu,\cos\theta_\nu,\phi_\nu,t)$, the emission and absorption rates for electron neutrinos R_e and R_a, and neutrino self-interaction potentials,

$$\mathcal{H}_{\nu\nu}=\sqrt{2}G_F\int\int\frac{E_\nu'^2dE_\nu'd\cos\theta_\nu'}{(2\pi)^2}\times(1-\cos\theta_\nu\cos\theta_\nu')\times(\rho_a(E_\nu',\cos\theta_\nu',t)-\bar{\rho}_a^*(E_\nu',\cos\theta_\nu',t)), \quad (6)$$

TABLE I. Numerical setup in this study. We refer to the SN simulation by Sumiyoshi and Yamada [71] ($r \sim 50$ km, 100 ms after the core bounce). The PTR-D model has the slightly smaller numbers of $\bar{\nu}_e$ and $\bar{\nu}_x$ and their number densities are shown in the parentheses.

ν flavor	$n_\nu/(10^{33}\ \mathrm{cm}^{-3})$	$T_\nu/(\mathrm{MeV})$	$\mu_\nu/(\mathrm{MeV})$	$R_a(30\ \mathrm{MeV})/(\mathrm{cm}^{-1})$	$R_e(30\ \mathrm{MeV})/(\mathrm{cm}^{-1})$
ν_e	1.28 (1.28)	4.5	0.0	2.0×10^{-5}	1.1×10^{-6}
$\bar{\nu}_e$	1.26 (1.16)	4.5	0.0	2.0×10^{-6}	1.1×10^{-7}
$\nu_x, \bar{\nu}_x$	6.28 (5.78)	6	−8.9	0.0	0.0

$$\bar{\mathcal{H}}_{\nu\nu} = \sqrt{2}G_F \int\int \frac{E_\nu'^2 dE_\nu' d\cos\theta_\nu'}{(2\pi)^2} \times (1-\cos\theta_\nu\cos\theta_\nu') \times (\rho_a^*(E_\nu',\cos\theta_\nu',t) - \bar{\rho}_a(E_\nu',\cos\theta_\nu',t)). \quad (7)$$

We refer to results of SN simulation by Sumiyoshi and Yamada [71] to the numerical setup. In detail, we focus on the situation of ∼50 km from the stellar center at 100 ms after the core bounce. The detailed parameters are summarized in Table I. In this situation, the chemical potentials of ν_e and $\bar{\nu}_e$ are almost zero and the necessary condition for FFCs is in place. In SN matter, the matter density decreases toward the stellar surface and neutrinos are decoupled from matter at a certain radius (neutrino sphere). The position of the neutrino sphere is generally $r_{\nu_e} > r_{\bar{\nu}_e} > r_{\nu_x},\ r_{\bar{\nu}_x}$, although it depends on neutrino energy. Here we focus on the region between the neutrino spheres of $\bar{\nu}_e$ and ν_x around average neutrino energy.[1] On the basis of this fact, we employ the initial energy spectrum of neutrinos in Fig. 1. Here the quantity on the vertical axis is defined as $I \equiv E_\nu^2/(2\pi)^3 \int \rho_a d\cos\theta_\nu$. It is assumed that ν_e and $\bar{\nu}_e$ are in the thermal equilibrium at all energies and at $E_\nu \gtrsim 20$ MeV, respectively. The energy spectrum for ν_e and the higher-energy part of $\bar{\nu}_e$ match with the FD of $T_\nu = 4.5$ and $\mu_\nu = 0$ MeV (dotted line). On the other hand, ν_x and $\bar{\nu}_x$ are already decoupled from matter at all neutrino energies in more of the inner region of the star. Therefore, ν_x and $\bar{\nu}_x$ spectra are consistent with the FD of $T_\nu = 6$ and $\mu_\nu = -8.91$ MeV (dot-dashed line) at high energies. It should be noted that the spectra of ν_e and ν_x are crossed with each other at $E_\nu \sim 25$ MeV.

We assume that ν_e are isotropic initially, while we use four anisotropic distributions for $\bar{\nu}_e$, ν_x, and $\bar{\nu}_x$, following the previous papers [49,55]. Hereafter, we call the angular distribution models from Shalgar and Tamborra [55] and Padilla-Gay *et al.* [49] the ST and PTR models, respectively. We define energy-integrated angular distributions as $g \equiv \int \rho_a E_\nu^2 dE_\nu/(2\pi)^3$,

$$g_{ee,0}(\cos\theta_\nu) = 0.5 n_{\nu_e},$$
$$\bar{g}_{ee,0}(\cos\theta_\nu) = \begin{cases} [0.47 + 0.05\exp(-(\cos\theta_\nu - 1)^2)] n_{\nu_e} & \text{(ST model)}, \\ \left[0.45 - a + \frac{0.1}{b}\exp\left(\frac{-(\cos\theta_\nu-1)^2}{2b^2}\right)\right] n_{\nu_e} & \text{(PTR model)}, \end{cases}$$
$$g_{xx,0}(\cos\theta_\nu) = \bar{g}_{xx,0}(\cos\theta_\nu) = 0.5\bar{g}_{ee,0}(\cos\theta_\nu). \quad (8)$$

where n_{ν_e} is the total number of electron neutrinos; a and b are angular-shape parameters in Table II. These initial angular distributions are shown in the top panel of Fig. 2. The bottom panel shows the angular distributions of ELN-XLN, or $L_e - L_x \equiv g_{ee} - \bar{g}_{ee} - g_{xx} + \bar{g}_{xx}$. All models have the angles with both of the positive and negative $L_e - L_x$, and hence FFCs are expected to be induced in all models. It should be noted that isotropic or nonisotropic in each flavor is consistent with whether or not the flavor is in thermal equilibrium.

The emission and absorption rates (R_e and R_a) are also adopted by reference to the same situation in the realistic SN simulation. For the reaction rate of ν_e, we emulate the electron capture by free protons, which is the dominant process in this situation. Specifically, we take $R_a(E_\nu) = 2\times10^{-5}\,\mathrm{cm}^{-1}(E_\nu/30\,\mathrm{MeV})^2$ and $R_e(E_\nu)$ is determined through the detailed balance relation, or $R_e(1-\rho_{ee,\mathrm{eq}}) = R_a\rho_{ee,\mathrm{eq}}$. Here $\rho_{ee,\mathrm{eq}}$ is the Fermi-Dirac distribution for ν_e with T_ν and μ_ν in Table I. For $\bar{\nu}_e$, the absorption rate is assumed to be $\bar{R}_a(E_\nu) = 0.1R_a(E_\nu)$, emulating the positron capture by free neutrons, and $\bar{R}_e(E_\nu)$ is determined through the detailed balance relation in the same manner as that for ν_e. We neglect the emission and absorption for ν_x and $\bar{\nu}_x$ except in Sec. III C.

We solve the QKEs with the Monte Carlo (MC) method [72]. This code can treat neutrino transport, matter collisions, and neutrino flavor conversions self-consistently. We ask readers to refer to [72] for more details.

[1]Specifically, we consider the transport sphere for ν_x and $\bar{\nu}_x$.

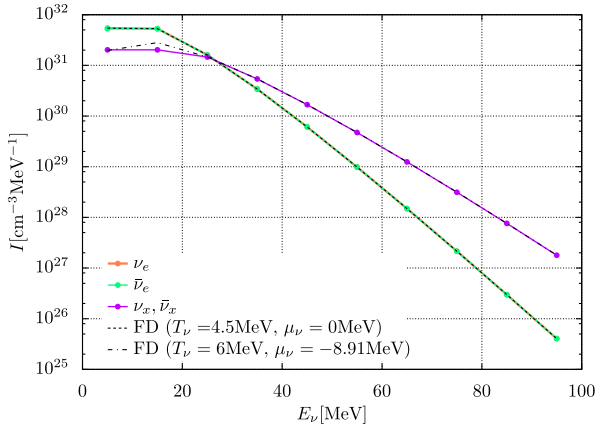

FIG. 1. Initial neutrino energy spectrum. Colors distinguish neutrino flavors. We also show the Fermi-Dirac distributions (FD) in black dotted ($T_\nu = 4.5$, $\mu_\nu = 0$ MeV) and dot-dashed lines ($T_\nu = 6$, $\mu_\nu = -8.91$ MeV).

III. MONOCHROMATIC NEUTRINOS

To extract the essence of emission and absorption effects, we first perform dynamical simulations of flavor conversions with a single neutrino energy. In Sec. III A, we investigate these effects using the PTR-B model, compared to the results in the absence of emission/absorption (PTR-Bwo). We also discuss how initial angular distributions and the emission/absorption of ν_x and $\bar{\nu}_x$ affect the results in Secs. III C and III B, respectively. Through this section, it is assumed that all neutrinos have $E_\nu = 13$ MeV, which is the typical average energy of ν_e in CCSNe. The total numbers of neutrinos for each flavor are shown in Table I and we adjust the energy bin width so that the initial ν_e distribution function matches the thermal equilibrium value. The emission and absorption rates for ν_e and $\bar{\nu}_e$ are set to be the values at $E_\nu = 13$ MeV and they satisfy the detailed balance relation at $T_\nu = 4.5$ and $\mu_\nu = 0$ MeV. We consider 128 propagation directions of neutrinos as a reference resolution, following the angular distributions in Eq. (8).

TABLE II. Parameters for initial angular distributions in the PTR models.

Model	a	b
PTR-B	0.02	0.4
PTR-C	0.02	0.6
PTR-D	0.06	0.2

A. General properties of neutrino emission and absorption effects

In this section, we explain effects of emission and absorption on flavor conversions using the PTR-B model. Figure 3 shows the time evolution of number densities for ρ_{ee} (top, solid), ρ_{xx} (top, dotted), and $\mathrm{Re}\rho_{ex}$ (bottom).

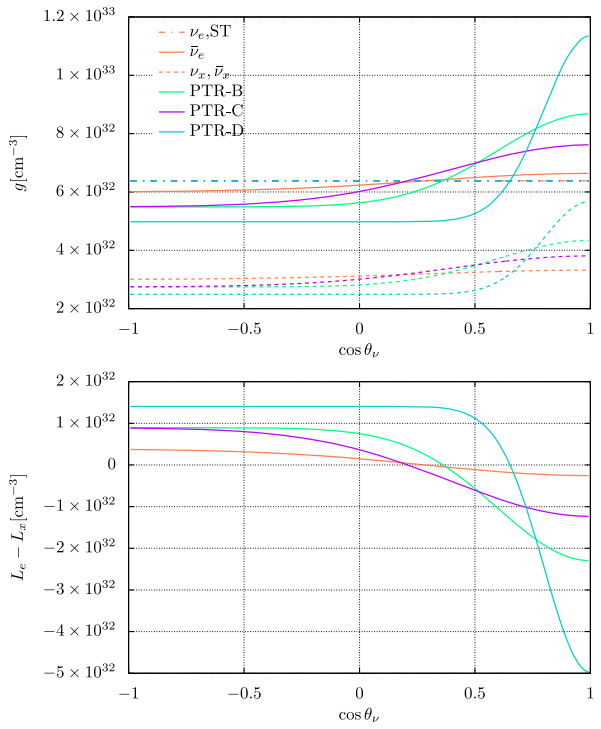

FIG. 2. Initial angular distributions (top) and ELN-XLN distributions (bottom). Colors and line types distinguish models and neutrino flavors, respectively.

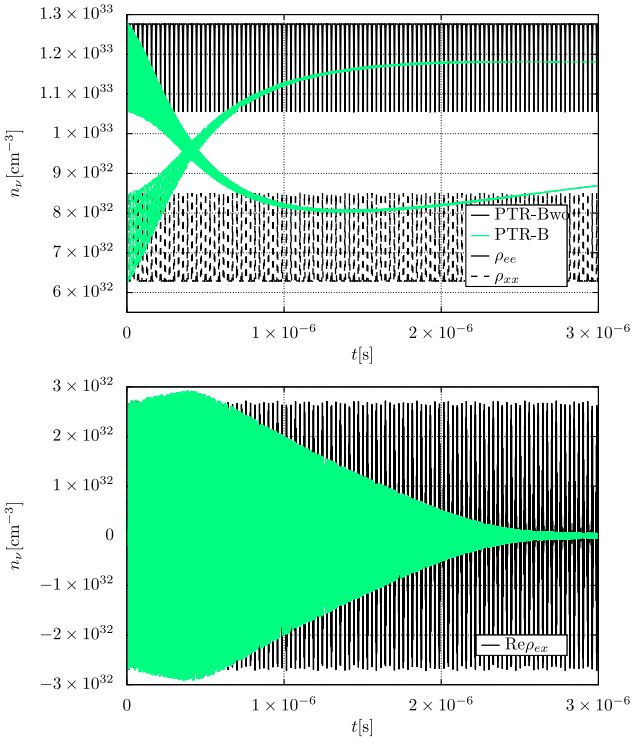

FIG. 3. Time evolution of number densities for ρ_{ee} (top, solid), ρ_{xx} (top, dotted), and $\mathrm{Re}\rho_{ex}$ (bottom). Green and black lines denote the PTR-B and PTR-Bwo models, respectively.

Green and black lines denote the PTR-B and PTR-Bwo models, respectively. In the PTR-Bwo model, the number densities of all components in the density matrix repeat increase and decrease periodically. This is the typical FFC dynamics under the homogeneous assumption, which is described in analogy with pendulum motions [55]. In the PTR-B model, on the other hand, emission and absorption break the symmetry of the pendulum motion, and the evolution of number densities is qualitatively different. This is the same as in the case of isoenergetic neutrino-matter scattering [50,51]. In detail, the number density of ν_e decreases until $t \sim 2 \times 10^{-6}$ s and then it starts to increase, while that of ν_x becomes almost constant after increase. This turning point is understood by the change of the driven mechanisms in the evolution. From here, we look at the detailed evolutionary properties in each phase.

In the early phase ($t \lesssim 2 \times 10^{-6}$ s), the evolution is driven by FFCs as well as the PTR-Bwo model, because the FFC timescale is much shorter than the collision one. Comparing with the PTR-Bwo model, however, the FFCs in the PTR-B model are more vigorous but shorter lived. More precisely, the FFCs are initially vigorous due to breaking the symmetry of the pendulum motion, while matter decoherence gradually attenuates the FFCs. After the competition between these two effects, the larger number of ν_e is converted to ν_x via FFCs. Before entering into the discussion in the nonlinear evolution, we check the results of the linear stability analysis. We numerically solve the linearized equations for Eqs. (4) and (5) with small perturbations for off-diagonal components. In the case without matter collisions, $\Gamma \equiv (R_e + R_a)/2$ and $\bar{\Gamma} \equiv (\bar{R}_e + \bar{R}_a)/2$ are set to be 0. The more detailed methods are described in the Appendix (see also [66]). Top and middle panels of Fig. 4 show the dispersion relation diagrams for the PTR-Bwo and PTR-B models, respectively. γ and ω_p denote the growth rate and oscillation frequency, respectively. The color bar describes the quantity of $|D|$ in Eq. (A14). The solutions of dispersion relations correspond to $|D| \sim 0$ (blue region). Among these solutions, the unstable (stable) modes correspond to those with $\gamma > 0$ ($\gamma \leqq 0$). For example, in the PTR-Bwo model, we find three blue regions and one unstable mode at $\omega_p \sim 0.2$ cm^{-1}. The exact values of γ and ω_p for the most unstable mode are summarized in Table III. It is found that γ for the PTR-B model is slightly larger than that for the PTR-Bwo model, but this is a small increase for the strong flavor conversions in the nonlinear phase. In other words, it seems difficult to predict nonlinear evolution from the linear phase study, incorporating emission and absorption. To see the vigor of FFCs in the nonlinear phase, the amplitudes of off-diagonal components (Reρ_{ex} and Imρ_{ex}) can be a good indicator. In the bottom panel of Fig. 3, the amplitude of Reρ_{ex} in the PTR-B model is larger than that in the PTR-Bwo model at $t \lesssim 5 \times 10^{-7}$ s. After this time, on the other hand, the amplitude decays by absorption [see the right-hand side of Eq. (4)], which indicates the suppression of FFCs. This attenuation moves to the latter phase or the collision driven phase ($t \gtrsim 2 \times 10^{-6}$ s).

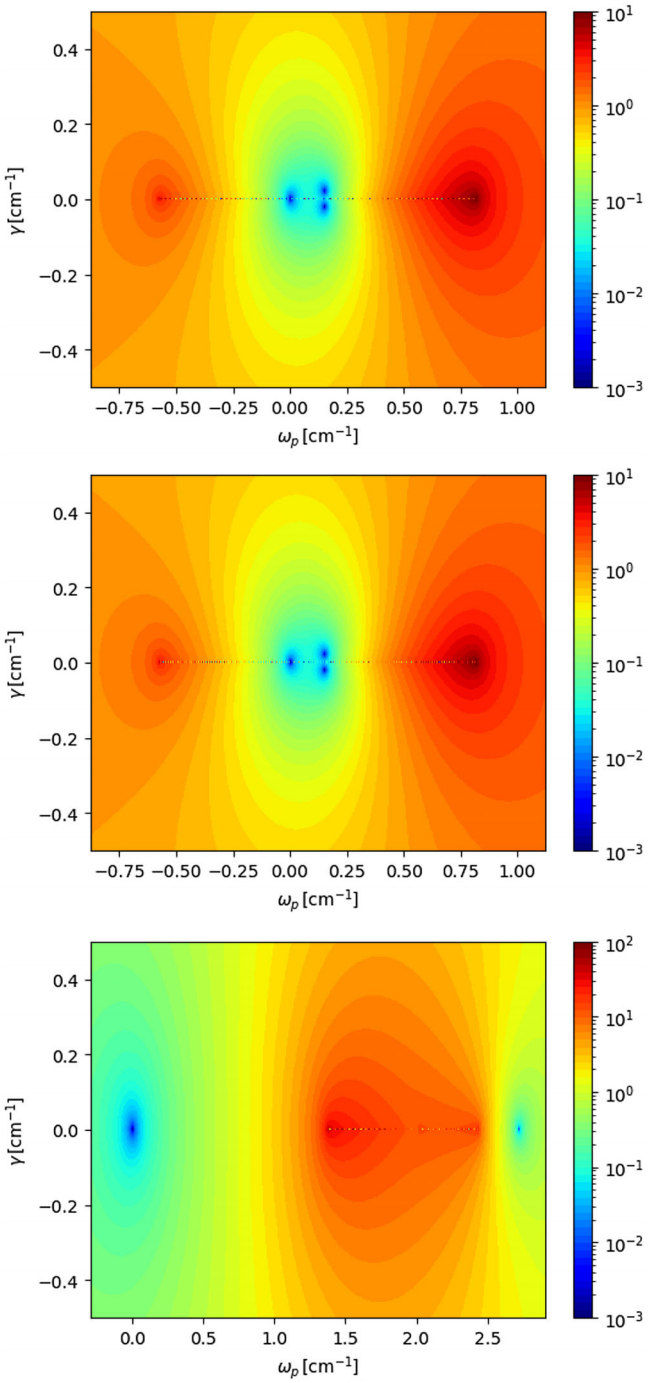

FIG. 4. Dispersion relation diagrams by the linear stability analysis. Top: the result of PTR-Bwo model at $t = 0$ s. The results of the PTR-B model are shown at $t = 0$ s (middle) and 8×10^{-6} s (bottom).

In the collision driven phase, CFIs and matter collisions characterize the evolution. Since the number of ν_x is almost constant, at first glance, it appears that no flavor conversion

TABLE III. Results of linear stability analysis at $t = 0$ and $t = 8 \times 10^{-6}$ s. The center dots $\cdots$ indicate that there are only solutions with $\gamma = 0$ of dispersion relations [Eq. (A14)].

	$t = 0$ s		$t = 8 \times 10^{-6}$ s	
Model	$\omega_p/(\mathrm{cm}^{-1})$	$\gamma/(\mathrm{cm}^{-1})$	$\omega_p/(\mathrm{cm}^{-1})$	$\gamma/(\mathrm{cm}^{-1})$
PTR-Bwo	0.150	2.11×10^{-2}		
ST($\Gamma = 0$)	0.167	4.01×10^{-3}	$\cdots$	$\cdots$
PTR-B($\Gamma = 0$)	0.150	2.11×10^{-2}	$\cdots$	$\cdots$
PTR-C($\Gamma = 0$)	0.155	9.56×10^{-3}	$\cdots$	$\cdots$
PTR-D($\Gamma = 0$)	0.952	0.182	$\cdots$	$\cdots$
ST	0.167	4.06×10^{-3}	1.55	7.40×10^{-8}
PTR-B	0.150	2.12×10^{-2}	2.72	2.12×10^{-6}
PTR-C	0.155	9.62×10^{-3}	2.36	2.38×10^{-6}
PTR-D	0.952	0.182	2.23	-5.20×10^{-6}
ST(multi)	0.167	4.02×10^{-3}	10.3	1.67×10^{-6}
PTR-B(multi)	0.150	2.12×10^{-2}	1.94	5.75×10^{-6}
PTR-C(multi)	0.155	9.58×10^{-3}	1.57	1.25×10^{-5}
PTR-D(multi)	0.952	0.182	1.84	5.88×10^{-5}

occurs. However, we find the unstable mode by the linear stability analysis at $t = 8 \times 10^{-6}$ s (see Table III and bottom panel of Fig. 4). The timescale of this mode is longer than that of interest, which accounts for the constant n_{ν_x}. To deepen the understanding, we also see the growth rate for the case of $\Gamma = 0$, employing the results of the PTR-B model [PTR-B($\Gamma = 0$)]. It should be noted that this model is different from the PTR-Bwo one. In the linear stability analysis, both models solve Eq. (A14) with $\Gamma = 0$, but the former uses the neutrino distributions obtained from numerical simulations with emission/absorption, while the latter uses the results without them. Figure 5 shows the enlarged dispersion relation diagrams without (left) and with (right) emission and absorption. In both cases, we have the solutions at $\omega_p \sim 2.718215$, but γ is almost 0 in the collisionless case, whereas γ is positive if collisions are taken into account. The exact values are summarized in Table III. This suggests that the unstable mode is a CFI. On the other hand, the number density of ν_e increases by emission until it will reach the thermal equilibrium with matter, or the initial state.

These features are also confirmed by the evolution of angular distributions. The left bottom panel of Fig. 6 shows the evolution of $L_e - L_x$ angular distributions in the PTR-B model. Different colors denote the different time steps. It is found that the crossing point moves toward $\cos\theta_\nu = 0$ and disappears at $2 \times 10^{-6} < t < 4 \times 10^{-6}$ s (cyan and yellow); this implies that FFCs are terminated during this time, which is consistent with the stability condition by the linear analysis (see left panel of Fig. 5). Figure 7 shows the evolution of g_{ee} (left) and g_{xx} (right). In the left bottom panel, we find that the angular distribution of ν_e deviates from the isotropic distribution by FFCs until $t \sim 2 \times 10^{-6}$ s and then it turns to the isotropization by emission. The angular distribution of ν_x, on the other hand, is not so evolved after $t = 2 \times 10^{-6}$ s (see right bottom panel) due to no emission and absorption processes. These features are also consistent with those in the number density evolution.

We find another interesting feature, or an angular swap, in Fig. 7. Top panels display the results of the PTR-Bwo model. Cyan lines denote the time step when the largest conversions occur near the $L_e - L_x$ crossing point ($\cos\theta_\nu \sim 0.1$), and it is found that g_{ee} (g_{xx}) at this angle is close to the initial g_{xx} (g_{ee}). The initial distributions are shown in black dotted lines. This feature is quite similar to a spectral swap observed in a slow instability [73]. It is known that the total lepton number ($\rho_{ee} + \rho_{xx}$) and the quantity of $P = (\rho_{ee} - \rho_{xx})^2 + 4(\mathrm{Re}\rho_{ex})^2 + 4(\mathrm{Im}\rho_{ex})^2$ are conserved in each propagation direction without matter

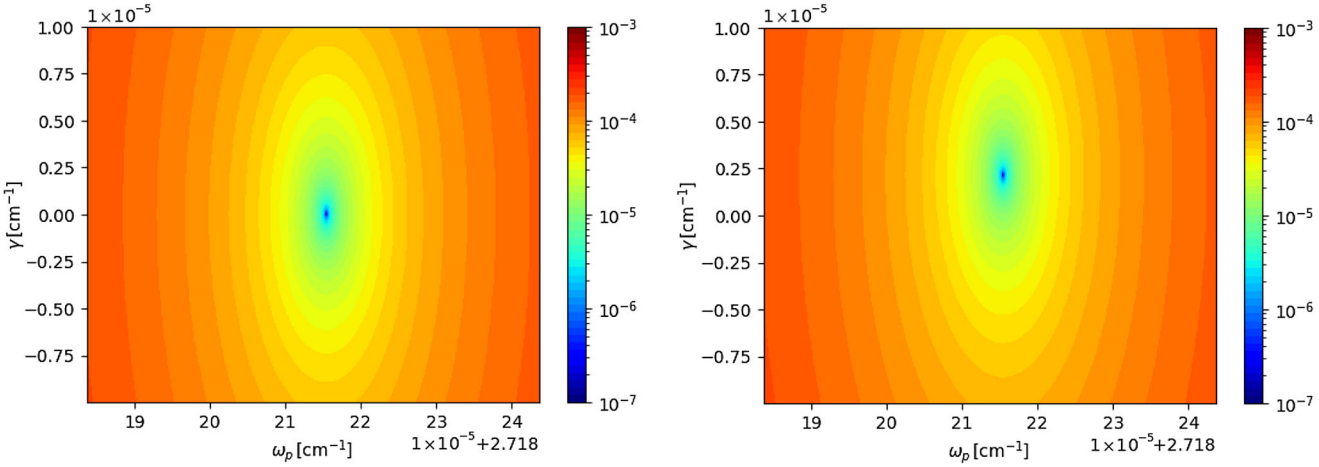

FIG. 5. Enlarged dispersion relation diagrams by the linear stability analysis for the PTR-B models at $t = 8 \times 10^{-6}$ s. Left/right: cases without and with emission and absorption, respectively. It should be noted that we use an enlarged label in the horizontal axis. For example, the value of 22 on the axis actually corresponds to $\omega_p = 2.71822$.

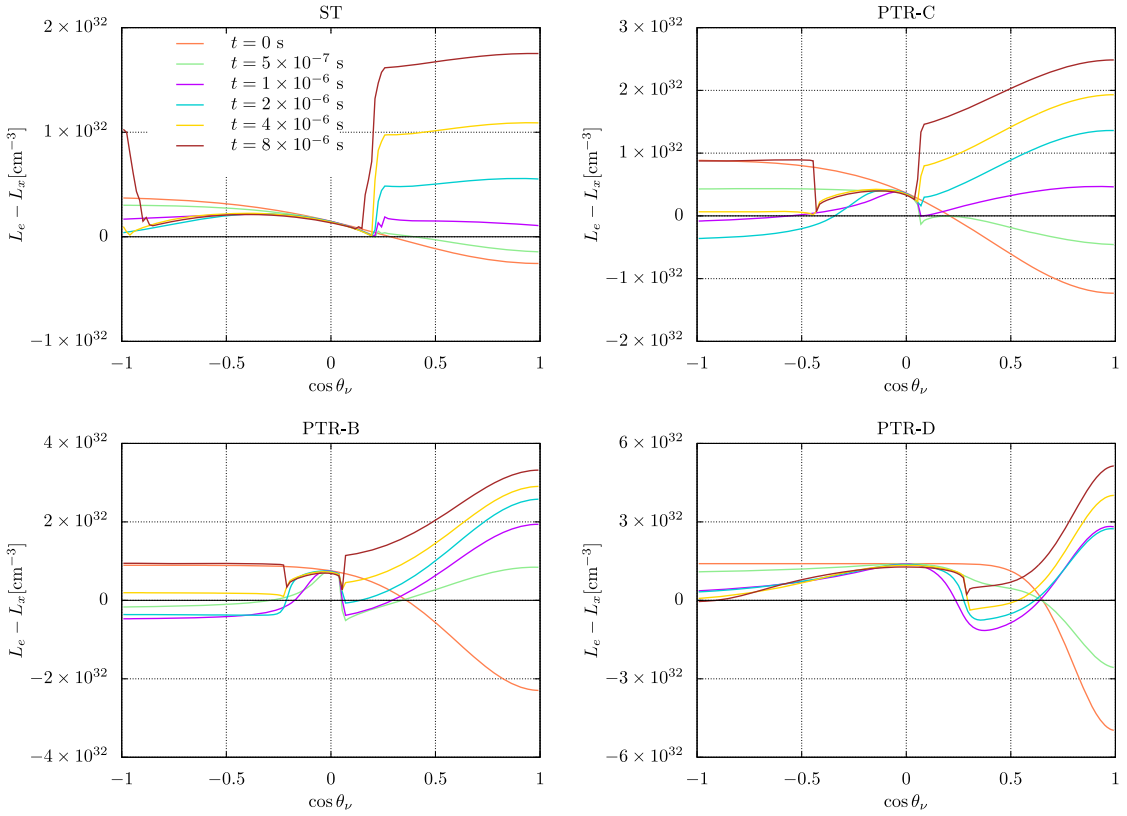

FIG. 6. Evolution of ELN-XLN angular distributions. Different colors denote the different time steps.

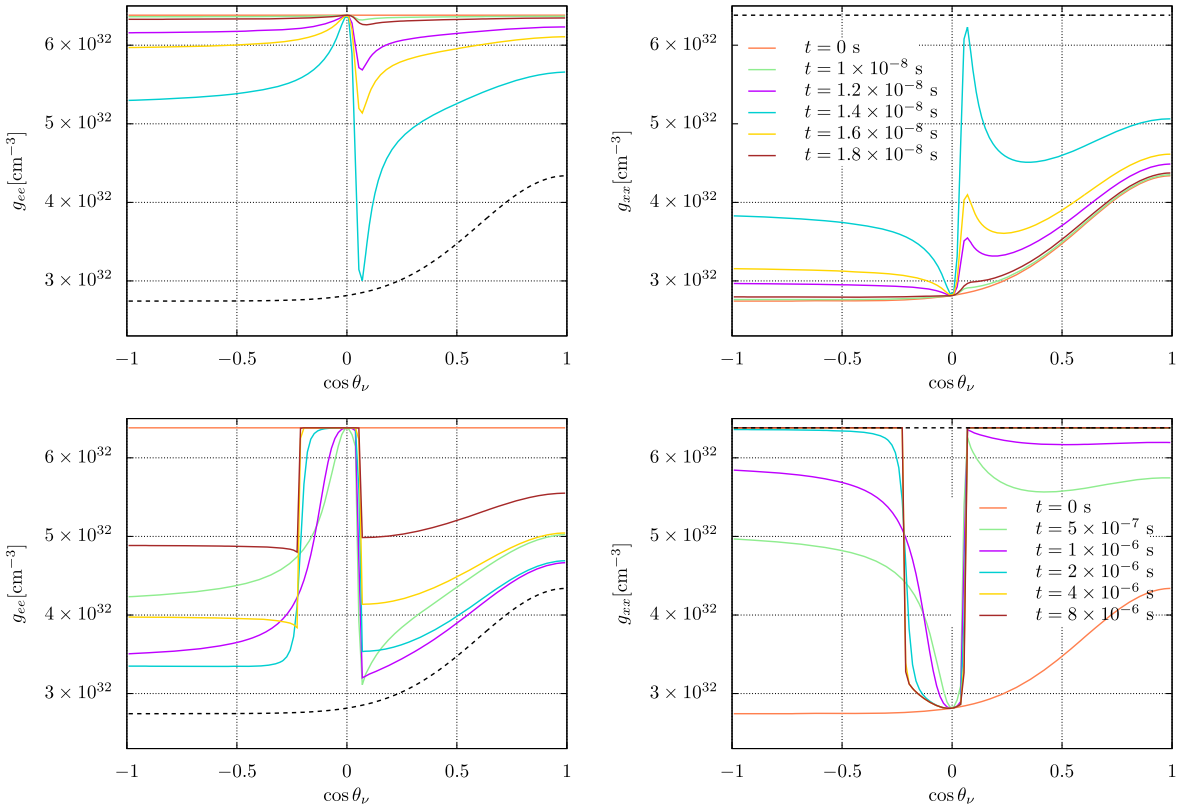

FIG. 7. Evolution of angular distributions in the PTR-Bwo (top) and PTR-B models (bottom). Left/right: results of ν_e and ν_x, respectively. Different colors denote the different time steps. The initial distribution of g_{xx} (g_{ee}) is plotted in black-dotted lines in g_{ee} (g_{xx}) panels.

collisions [74].[2] From these quantities, we derive that g_{ee} and g_{xx} cannot change beyond each other's initial values. Including neutrino emission and absorption, the angular swaps are found at the wider angles (see bottom panels). Matter collisions shift the $L_e - L_x$ crossing points slightly with time as seen in Fig. 6. On the other hand, since the collision timescale is much longer than that for FFCs, matter collisions can be neglected while FFCs are occurring and the similar large conversions at the new crossing points occur as the case of pure FFCs. This is the reason for the more vigorous FFCs in the PTR-B model than those in the PTR-Bwo model. Thus, it is worth noting that matter collisions that are sufficiently slower than FFCs have a significant impact on the dynamics of FFCs.

B. Dependence of initial angular distribution

It is known that angular distributions are one of the essential factors for the dynamics of FFCs [49]. Moreover, impact of matter collisions also depends on the degree of anisotropy of neutrinos. Hence, we discuss the dependence of initial angular distributions in this section. We employ four models with different angular distributions: ST and PTR models [see Eqs. (8) and Fig. 2]. They have different ELN-XLN crossing points in the bottom panel of Fig. 2 and the order of crossing depth is the PTR-D > PTR-B > PTR-C > ST model. Figure 8 shows the dispersion relation diagrams for the ST (top), PTR-C (middle), and PTR-D (bottom) models at $t = 0$ s, and the ω_p and γ of unstable modes are summarized in Table III. It is found that the growth rate is in line with the crossing depth. This is consistent with the previous studies [49].

Figure 9 shows the time evolution of number densities. The description is the same as Fig. 3. We find that all models have two phases with the different driven mechanisms of evolution: FFC and matter collision driven phases, but the evolution features in each phase are different among models. In the FFC driven phase ($t \lesssim 4 \times 10^{-6}$ s), the features of n_{ν_x} evolution, i.e., the oscillation amplitude, vigor, and lifetime of FFCs, depend on the initial angular distributions, as expected from the results of linear stability analysis (see Table III). In particular, it is found that the numbers of ν_x produced via FFCs are not correlated with the initial growth rate. For example, the PTR-D model has the largest growth rate, whereas the final sate of n_{ν_x} is smallest among the models. This is due to the nonlinear interplay between FFCs and matter collisions. From the previous discussion, it follows that the crossing depth in the initial angular distribution is also not an appropriate indicator of the nonlinear evolution. This is consistent with the previous studies without matter collisions but with inhomogeneous neutrino background [14,61].

In the collision driven phase ($t \gtrsim 4 \times 10^{-6}$ s), n_{ν_e}'s in all models increase by emission along with the attenuation of

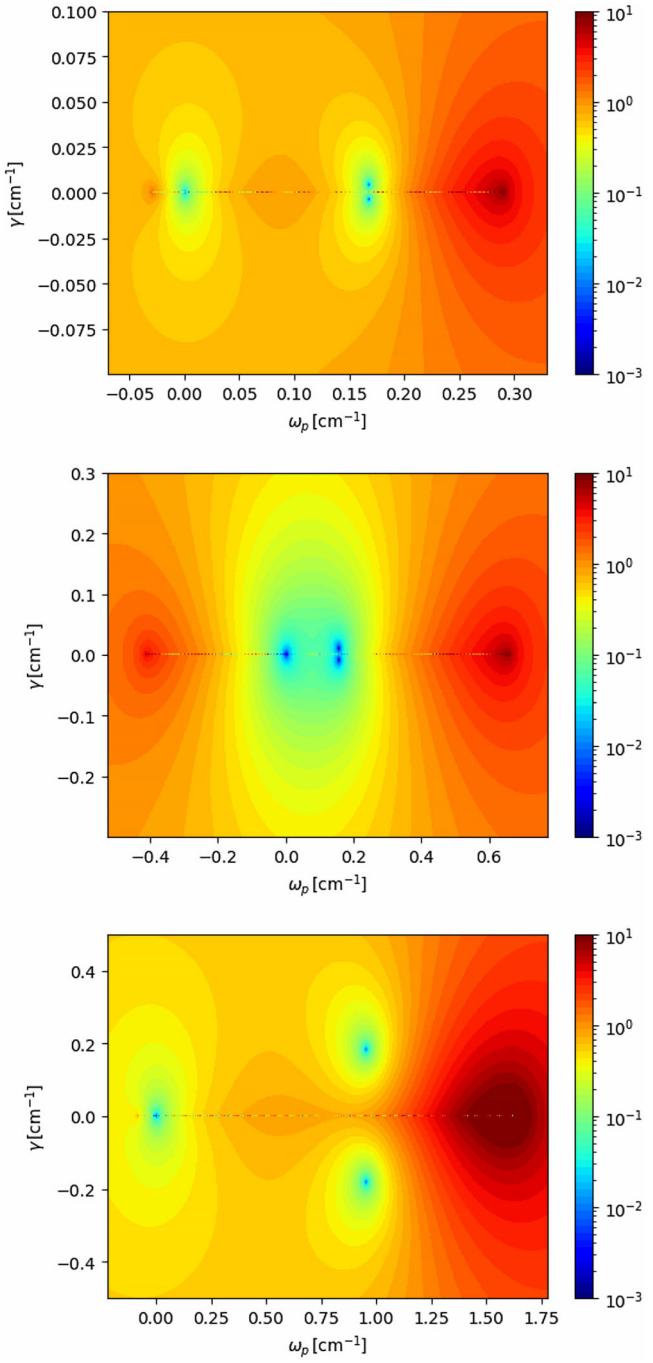

FIG. 8. Dispersion relation diagrams by the linear stability analysis at $t = 0$ s. The results of ST, PTR-C, and PTR-D models are shown from top to bottom, respectively.

FFCs. On the other hand, the ν_x evolution is different among models. This shows the difference in the behavior of flavor conversions. First, we see the results of linear stability analysis. γ's at $t = 8 \times 10^{-6}$ s are summarized in Table III. We find that the models other than the PTR-D model have unstable modes. Since these modes disappear in the collisionless cases (see the results of the $\Gamma = 0$ cases in Table III), they are CFIs. In the PTR-D model, we have

[2] P corresponds to the length of polarization vector.

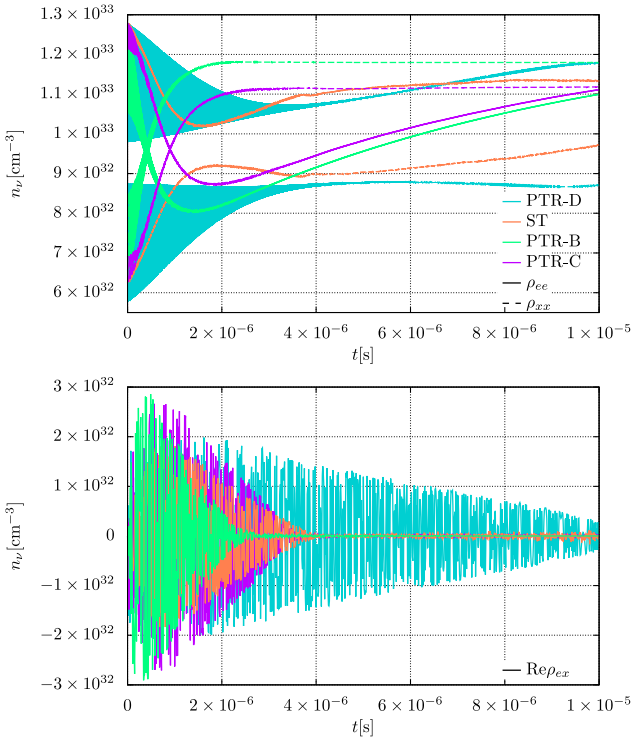

FIG. 9. Time evolution of number densities for ρ_{ee}, ρ_{xx} (top) and $\mathrm{Re}\rho_{ex}$ (bottom). Colors and line times distinguish the models and neutrino flavor, respectively.

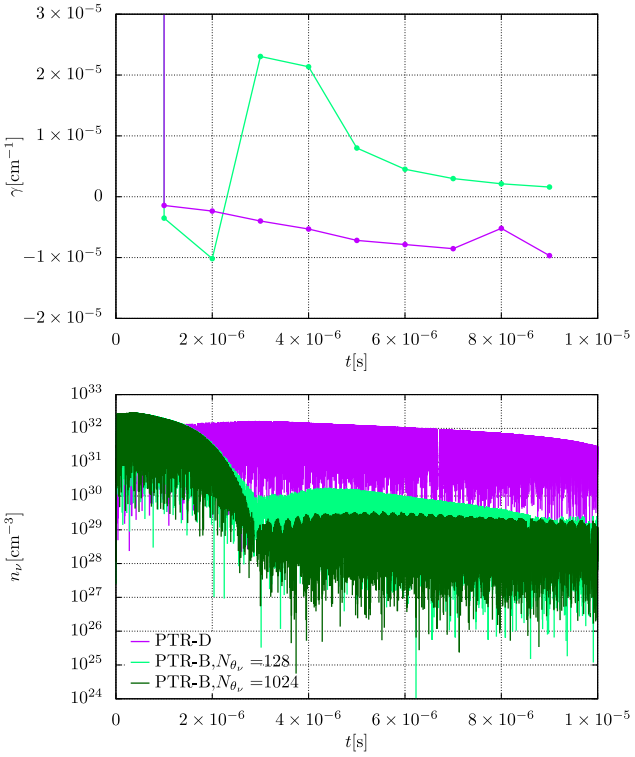

FIG. 10. Time evolution of growth rate (top) and $\mathrm{Re}\rho_{ex}$ (bottom) for the PTR-B and PTR-D models. Colors distinguish the models. It should be noted that the bottom panel uses the same data as the bottom panel of Fig. 9, but the vertical axis is drawn in log scale.

only the solution with $\gamma < 0$ and flavor conversions decay by the matter decoherence. The matter decoherence features can be read from the evolution of $\mathrm{Re}\rho_{ex}$. To qualitatively understand the decoherence, we see the time evolution of γ in the PTR-B and PTR-D models. The results are shown in the top panel of Fig. 10. In the bottom panel, we also replot the $\mathrm{Re}\rho_{ex}$ evolution of Fig. 9 in the logarithmic scale for convenience. In the former (green), at $1 \times 10^{-6} < t < 2 \times 10^{-6}$ s, γ becomes negative, which implies that the initially induced FFCs are attenuated by the matter decoherence. After the attenuation of FFCs, γ comes back to positive because of the CFIs. These trends of γ evolution match with those of $\mathrm{Re}\rho_{ex}$ in the bottom panel, including the timescale of increase/decrease. In the PTR-D model, once γ becomes negative at $t = 1 \times 10^{-6}$ s, it stays throughout the simulation time. That indicates that the matter decoherence continues in the later phase. We find that this is again consistent with the $\mathrm{Re}\rho_{ex}$ evolution. Thus, the γ evolution can be a useful tool to capture the evolutional trend of off-diagonal components.

The evolution of $L_e - L_x$ distributions is shown in Fig. 6. They also suggest the same features as those in the number density evolution of each model. In the PTR-C models (right top), $L_e - L_x$'s are positive in all directions at $t \gtrsim 4 \times 10^{-6}$ s (yellow). This is consistent with the saturation timescale in the n_{ν_x} evolution. Moreover, FFCs no longer occur after this time as well as the linear analysis suggests. In the PTR-D model (right bottom), the negative $L_e - L_x$ is found at $\cos\theta_\nu \sim -1$, even at $t = 8 \times 10^{-6}$ s, but the crossing is so small that the matter decoherence dominates over flavor conversions. In the ST model, although $L_e - L_x$'s are positive at all directions after $t \sim 10^{-6}$ s and the results seem to be understandable through similar considerations, we must take care of the angular resolution, as described below.

Finally, we should note the importance of angular resolution. We perform the resolution study and find that the results need attention only with respect to the ST model. Its n_{ν_x} evolution is shown in Fig. 11. Different colors denote different number of angular grids, or N_{θ_ν}. It is found that the increment of n_{ν_x} in the later phase ($t \gtrsim 6 \times 10^{-6}$ s) becomes more gradual with the angular resolution. This is because the fine structure is not accurately resolved in the case of low resolution and, moreover, the spurious unstable modes artificially enhance the evolution [75]. This fact again makes us aware of the importance of the angular distribution in FFCs. It should be noted that we confirm the reference resolution with $N_{\theta_\nu} = 128$ is sufficient in the other models.

C. Emission and absorption of ν_x and $\bar{\nu}_x$

ν_x and $\bar{\nu}_x$ also interact with surrounding matter via thermal processes in CCSNe and BNSMs, although their reaction rates are smaller than those of ν_e and $\bar{\nu}_e$.

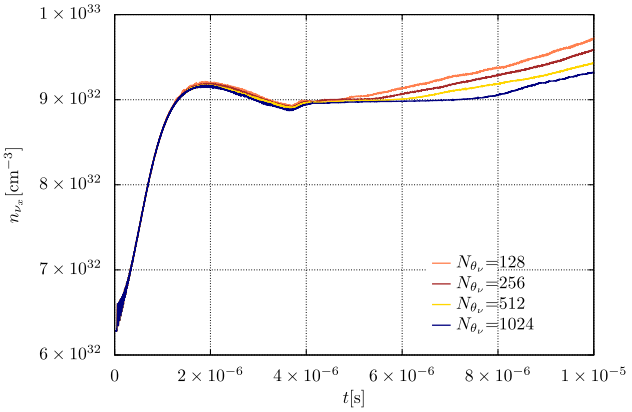

FIG. 11. The resolution study of n_{ν_x} evolution in the ST model. Colors distinguish the number of angular grids.

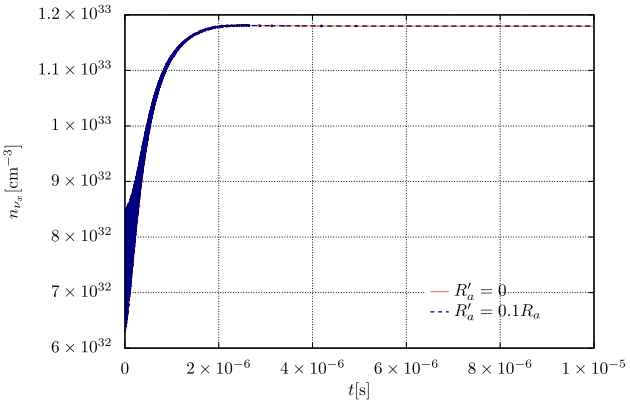

FIG. 12. The n_{ν_x} evolution in the cases of $R'_a = 0$ (coral, solid) and $0.1R_a$ (navy, dotted). We employ the PTR-B model as the initial angular distributions.

If emission and absorption of ν_x and $\bar{\nu}_x$ are taken into account, they are also thermalized as well as ν_e and the evolution of n_{ν_x} may be changed. We hence investigate effects of emission and absorption for ν_x and $\bar{\nu}_x$ in this section. The collision term C, or the second term on the right-hand sides of Eq. (4), is written as

$$C = \begin{pmatrix} 2\pi R_e - [R_e + R_a]\rho_{ee,a} & -\frac{1}{2}[R_e + R_a + R'_e + R'_a]\rho_{ex,a} \\ -\frac{1}{2}[R_e + R_a + R'_e + R'_a]\rho_{xe,a} & 2\pi R'_e - [R'_e + R'_a]\rho_{xx,a} \end{pmatrix}, \tag{9}$$

with the ν_x emission and absorption rates R'_e and R'_a. For antineutrinos, the same reaction rates are introduced into $\bar{C}$ in the same manner. The absorption rates are set to be $R'_a = 0.1R_a$ and the emission rates are determined by the detailed balance relation with $T_\nu = 4.5$ and $\mu_\nu = 0$ MeV. The angular distributions in the PTR-B model are employed initially. Figure 12 shows the n_{ν_x} evolution. Coral and navy lines denote the cases of $R'_a = 0$ and $0.1R_a$, respectively. We find that the deviation from the case of no ν_x emission and absorption processes is $\sim 5 \times 10^{-3}\%$ at $t = 10^{-5}$ s, owing to the slow collision timescale ($\sim 1.6 \times 10^{-3}$ s). It is confirmed that thermalization effects for $\nu_x/\bar{\nu}_x$ are negligible unless their reactions become comparable to ν_e and $\bar{\nu}_e$.

IV. NONMONOCHROMATIC NEUTRINOS

In CCSNe and BNSMs, neutrinos have nonmonochromatic energy spectrum and the reaction rates of neutrino-matter interactions are energy dependent. Hence, it is natural to consider the evolution of neutrino flavors with matter collisions in the multienergetic treatment. In this section, we employ the neutrino energy spectrum and the energy-dependent reaction rates into numerical simulations. The initial energy spectra are described in Fig. 1 and they are consistent with the realistic CCSN simulation. We adopt ten energy meshes in the range of 0–100 MeV. As the single-energy case, the energy-integrated angular distributions follow Eqs. (8) of four models (see also Fig. 2) and the same numbers of neutrinos are employed in Table I. We distribute 1280 MC samples in a neutrino phase space.

Figure 13 shows the time evolution of n_{ν_e} (top) and n_{ν_x} (bottom). Colors distinguish the models, and the results of single-energy cases are also plotted in darker dotted lines. We find that this evolution has two phases, FFC and collision driven phases, the same as the single-energy case. First, we discuss effects of multienergetic treatment using the PTR-B model as a reference (green). At $t \lesssim 4 \times 10^{-6}$ s, FFCs drive the evolution as well as the single-energy case. Table III shows the results of linear stability analysis. We find that the growth rate is almost the same as that in the single-energy case. This fact is attributed to the property that the dynamics of pure FFCs is energy independent and depends on the number densities of neutrinos [see Eq. (4)]. On the other hand, the overall flavor evolution is delayed by effects of energy-dependent collisions. For $E_\nu \lesssim 13$ MeV, the reaction rates are smaller than that in the single-energy case, and decoherence by the absorption of off-diagonal components is weak. As seen in Fig. 1, the fraction of neutrinos with $E_\nu \lesssim 13$ MeV to the total number of neutrinos is $\sim 84\%$ initially and these neutrinos contribute to the self-interaction Hamiltonian $H_{\nu\nu}$. This dominancy of low-energy neutrinos leads to the slower attenuation of FFCs, and hence the lifetime of FFCs is extended in the multienergy treatment.

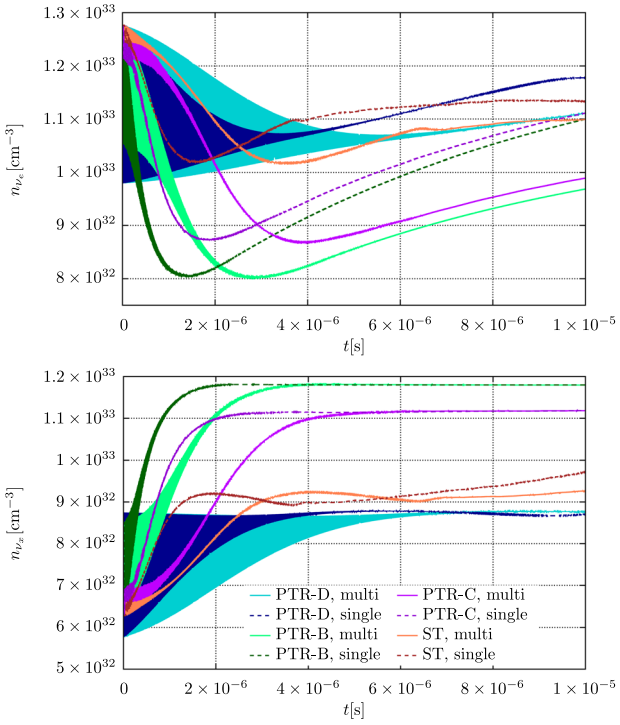

FIG. 13. Time evolution of n_{ν_e} (top) and n_{ν_x} (bottom) in the case of multienergy. Colors distinguish the angular models and the results of single-energy cases are also plotted in darker dotted lines.

The extension of FFC lifetime is also confirmed by the evolution of $L_e - L_x$ evolution in the left bottom panel of Fig. 14. The multi- and single-energy results are shown in solid and dashed lines, respectively. At $t = 4 \times 10^{-6}$ s, $L_e - L_x$'s are positive at all angles in the single-energy case, whereas the negative $L_e - L_x$ appears at $\cos\theta_\nu \lesssim -0.2$ in the multienergy case. This indicates that FFCs in the multienergy case still survive until this time. The crossings in this case disappear at $t = 8 \times 10^{-6}$ s.

In our previous paper [56], we proposed the χ diagnostics to quantify the impact of multienergy effects on FFCs with a χ parameter, or $\chi = |(\langle E_\nu\rangle - \langle RE_\nu\rangle)/(\langle E_\nu\rangle + \langle RE_\nu\rangle)|$. $\langle E_\nu\rangle$ and $\langle RE_\nu\rangle$ are the average energy of neutrinos and the reaction-weighted one, respectively. In the monochromatic neutrino case, χ exactly becomes 0. If $\chi \sim 0$ in the multienergy case, neutrinos with a particular energy dominantly contribute to a flavor evolution and results are close to single-energy ones. As χ increases, the deviation from single-energy results becomes larger, and the multienergy treatment is essential. We derive $\chi = 0.281$ for the PTR-B model, which indicates that the multienergy treatment is essential in this model. This is consistent with numerical results.

Similar to scatterings, the energy-dependent emission/absorption generates rich energy-dependent features in FFCs. Figure 15 shows the time evolution of I_{ee} (blue)

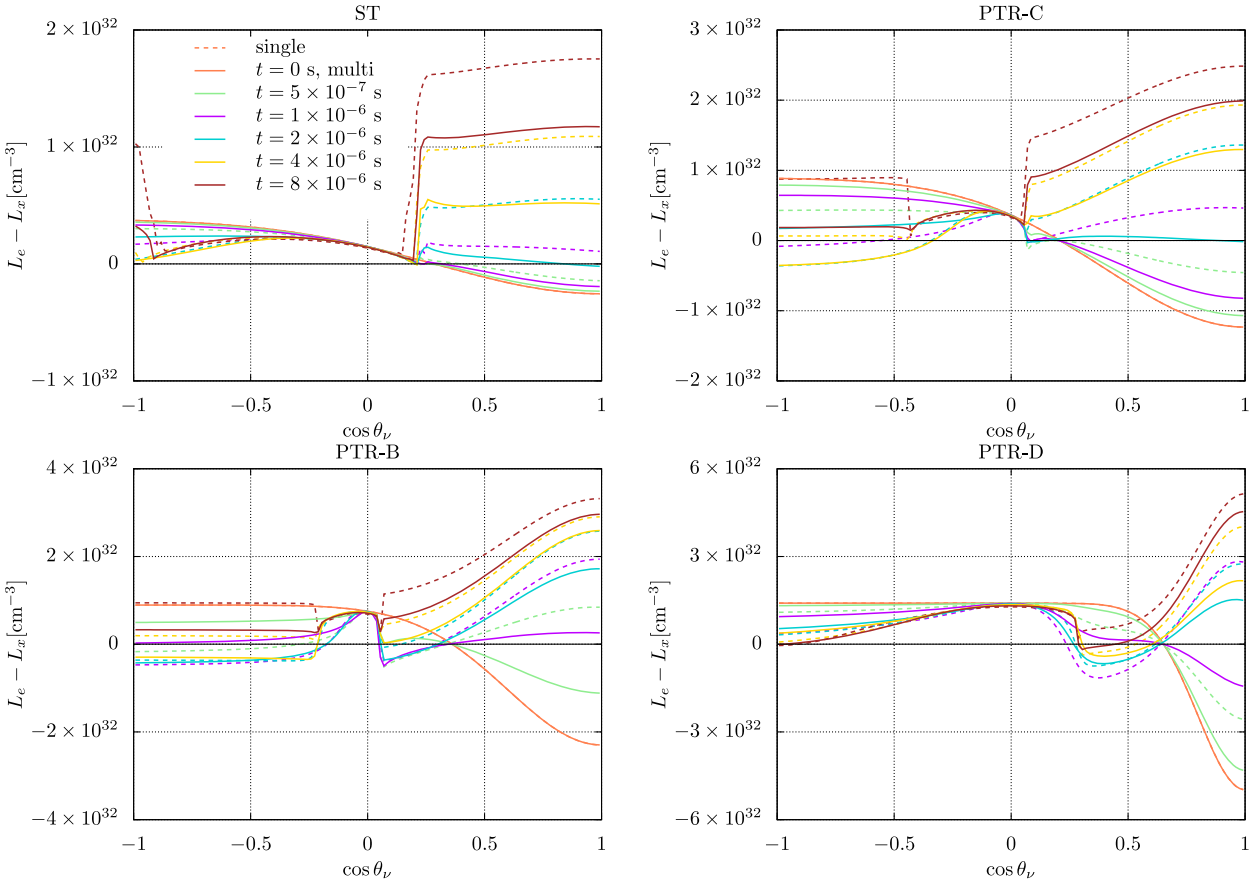

FIG. 14. The same figures as Fig. 6, but for the multienergy case.

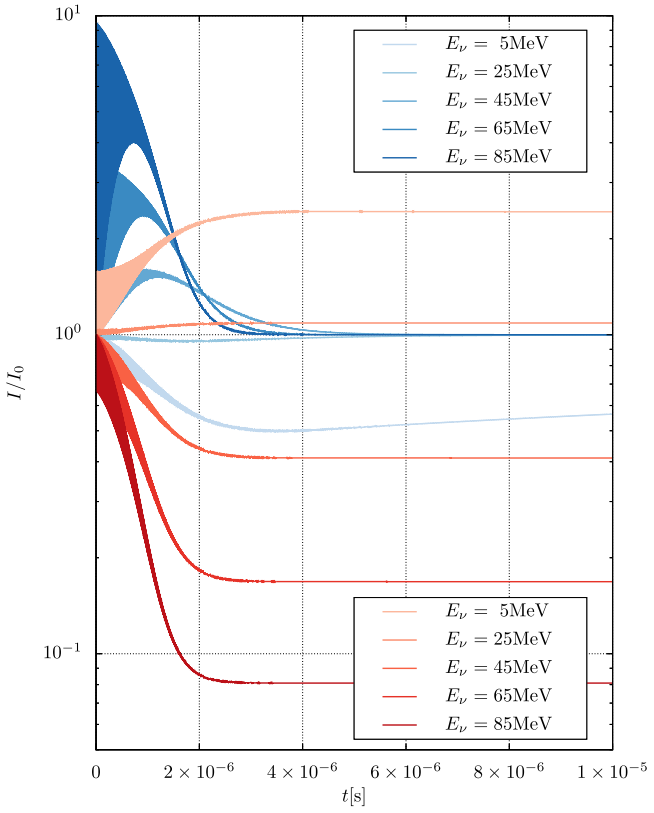

FIG. 15. Time evolution of I_{ee} (blue) and I_{xx} (red) in the PTR-B model. We normalize I's by the initial values I_0's in each neutrino energy. Colors get darker with neutrino energy.

and I_{xx} (red). We normalize I's by the initial values I_0's in each neutrino energy. Colors get darker with neutrino energy. It is found that $I_{ee}/I_{ee,0}$'s for $E_\nu \lesssim 25$ MeV increase with time, whereas they decrease for $E_\nu \gtrsim 25$ MeV. This is attributed to the initial spectral crossing between I_{ee} and I_{xx} at $E_\nu \sim 25$ MeV (see Fig. 1). Since FFCs attempt to eliminate the difference between ν_e and ν_x, the direction of conversions differs between high and low energies. Related to this, we find that flavor conversions occur strongly at the higher energy because of the larger difference between I_{ee} and I_{xx}.

In the late phase ($t \gtrsim 4 \times 10^{-6}$ s), after FFCs are sufficiently attenuated, matter collisions and CFIs drive the evolution. In top panel of Fig. 13, we find that n_{ν_e} increases by emission more slowly than the single-energy case. This indicates the energy-averaged emission rate is smaller in the multienergy case, which is consistent with the result in the FFC driven phase. On the other hand, since reactions for ν_x and $\bar{\nu}_x$ are neglected, the constant evolution is observed as the same as the single-energy case. As shown by the linear stability analysis, the unstable mode is observed at $t = 8 \times 10^{-6}$ s, but the growth rate γ is longer than the timescale of interest (see Table III). Considering that the crossings in the $L_e - L_x$ distribution disappear at $t = 8 \times 10^{-6}$ s, this unstable mode is presumed to be CFIs. Moreover, it should be noted that the asymptotic values of n_{ν_x} are nearly identical between the single- and multienergy cases. This is understood by the evolution of angular distributions in Fig. 16. We find the angular swaps between ν_e and ν_x at wider angular range the same as the single-energy case. As mentioned in Sec. III A, FFCs at each angle are determined by the total lepton number and the quantity P. Since adopting the same angular distributions for both cases, the asymptotic states are almost the same.

We also investigate the dependence of initial angular distributions using the ST and PTR models. In all the models, the initial growth rates γ are almost the same as the single-energy case in Table III, which again describes the property of FFCs. The results in the nonlinear phase are shown in Figs. 13 and 14. In all models, the overall evolution becomes slower than the single-energy cases as the same as the PTR-B model, while the features of each model are similar to those of the single-energy case. Below are some comments on individual models. The effects of

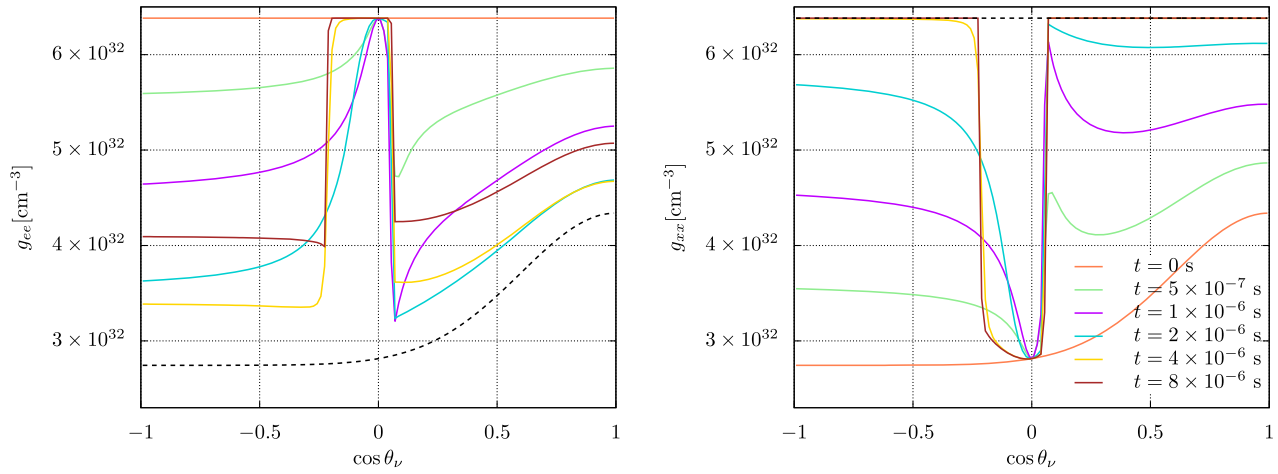

FIG. 16. The same as Fig. 7, but for the multienergy case.

multienergy treatment in the PTR-C model are similar to that in the PTR-B model. Specifically, the asymptotic states in the PTR-C model ($t \gtrsim 4 \times 10^{-6}$ s) are almost identical between the single- and multienergy cases due to the fact that the maximum amount of FFCs is limited. After the $L_e - L_x$ crossing disappears at $t \sim 8 \times 10^{-6}$ s, CFIs drive the weak flavor conversions. In the PTR-D model, the $L_e - L_x$ crossings are still observed even at $t = 8 \times 10^{-6}$ s in Fig. 14 and FFCs survive to the end in the timescale of interest. As the same as in the single case of the ST model, high angular resolutions are necessary in the multienergy case. In the high-resolution results ($N_{\theta_\nu} = 512$), the $L_e - L_x$ crossings are found even at $t = 8 \times 10^{-6}$ s, and hence the unstable mode at this time may be the weak FFCs.

V. SUMMARY AND DISCUSSION

We perform dynamical simulations of neutrino flavor conversions with neutrino emission and absorption under the assumption of homogeneous neutrinos. We adopt a physically motivated setup in this study, which is set based on the results of realistic SN simulations [71]. We start by discussing the case with energy-independent reaction rates (Sec. III), which presents some key features of the interplay between flavor conversion and emission/absorption. The dynamics is qualitatively different from FFCs without collisions; indeed, the periodic (or pendulumlike) features in flavor conversions disappear. The result is essentially in line with the case with isoenergetic neutrino-matter scattering [50,55,56].

We also find that the time evolution of flavor conversions with emission/absorption can be divided into two phases, (1) the FFC driven phase and (2) a collisional one. The multiple phase appearing in the nonlinear regime is accounted for by the disparity of timescales between FFCs and collisions. In the former phase, FFCs are initially more vigorous than the case without collisions due to breaking the symmetry of pendulum motion by collisions. On the other hand, FFCs are gradually attenuated by matter decoherence. After the competition of these collision effects, the larger number of ν_e is converted to ν_x by FFCs. In the latter phase, the flavor conversion is driven by CFIs, while the timescale is much longer than FFCs. ν_e and $\bar{\nu}_e$, which are less populated than the initial states due to strong FFCs in the earlier phase, are replenished by emission. The asymptotic states are characterized by matter collisions in this phase. Although the detailed features depend on the initial condition, we show that the overall trend is similar among all our models. It should also be worthy to note that ν_x emission/absorption does not change our conclusion, unless their reactions become comparable to ν_e and $\bar{\nu}_e$.

We also find that angular swap between ν_e ($\bar{\nu}_e$) and ν_x ($\bar{\nu}_x$) is facilitated by emission/absorption. In the pure FFC cases, the swap occurs in a very narrow angular region where ELN crossing occurs nearby. On the other hand, the crossing point can substantially deviate from the initial angular position in the case with emission/absorption, which expands the region where the angular swap occurs.

We extend our discussion in the case with energy-dependent reaction rates. The initial energy spectra are set so as to be consistent with realistic SN simulations. In the low-energy regime, the isotropization of neutrinos by emission/absorption is less remarkable, and therefore the lifetime of FFCs can be longer than the single-energy case. As a result, the overall trend becomes similar to the case with the lower reaction rate for monochromatic neutrinos. It should be mentioned that, although the flavor conversion is less vigorous than the single-energy case, the long-lived FFCs compensate for this. In fact, the degree of flavor conversion is almost identical to the single-energy case, and the angular swap is also observed in a wide angular region. We also find that the energy-dependent emission/absorption generates rich energy-dependent features in FFCs similar to scatterings. In the initial condition, the energy spectra of ν_e and ν_x are comparable at $E_\nu \sim 25$ MeV, while ν_e and ν_x are dominant at the lower- and higher-energy regions, respectively. This shows that the increase or decrease of each flavor of neutrinos due to flavor conversion becomes qualitatively different between the low- and high-energy region.

Although the present study does not address all issues in the interplay between flavor conversions and collision terms, it provides some valuable insights on quantum kinetic features of neutrinos in CCSN and BNSM environments. One of them is to determine asymptotic states of neutrinos. As shown in our models, FFCs promptly establish a quasisteady state, which corresponds to, however, just a *pseudo* asymptotic state. After FFCs subside, matter collisions or CFIs take over to dictate secure evolution of neutrinos, asymptoting to another state. This indicates that the actual asymptotic state of neutrinos cannot be determined solely by either neutrino flavor conversion or neutrino-matter interaction, but by self-consistent treatments of feedback between both of them.

This study also reveals a new possibility that flavor conversion offers a new path to absorb ν_x in the high-energy region. Since the ν_x is initially larger than ν_e, flavor conversions facilitate the ν_x conversion to ν_e, and then it is absorbed through charged-current reactions of ν_e, exhibiting an increase of neutrino heating. It is an intriguing question how the heating can influence CCSN and BNSM dynamics, although we leave the detailed investigations for future work.

In this work, we impose many simplifications and assumptions, such as homogeneous neutrino gas, axial symmetry in momentum space, and a two flavor system. Recent works have shown that the dynamics of flavor conversion is very sensitive to these conditions (e.g., [13,14,38,40,42,61,76,77]). We also note that the

homogeneous approximation suffers from a self-consistent problem in studying the impact of collisions on flavor conversion [78]. It should be stressed, however, that some intrinsic features of collision effects can be studied in our simplified approach. This offers new insights into roles of flavor conversions on CCSNe/BNSMs dynamics.

ACKNOWLEDGMENTS

We are grateful to Lucas Johns for useful comments and discussions. C. K. is supported by JSPS KAKENHI Grants No. JP20K14457 and No. JP22H04577. M. Z. is supported by JSPS Grant-in-Aid for JSPS Fellows (No. 22J00440) from the Ministry of Education, Culture, Sports, Science and Technology (MEXT), Japan. The numerical calculations were carried out on Cray XC50 at Center for Computational Astrophysics.

APPENDIX: LINEAR STABILITY ANALYSIS

In the linear stability analysis, we focus on the off-diagonal components S and $\bar{S}$ of neutrino density matrices,

$$\rho = \begin{pmatrix} \rho_{ee} & S \\ S^* & \rho_{xx} \end{pmatrix}, \qquad \bar{\rho} = \begin{pmatrix} \bar{\rho}_{ee} & \bar{S} \\ \bar{S}^* & \bar{\rho}_{xx} \end{pmatrix}. \tag{A1}$$

In the flavor-isospin convention, in which negative energy stands antineutrinos as $\bar{\rho}(E) \equiv -\rho(-E)$, the governing equation for the off-diagonal component can be written from Eqs. (4) and (5) as

$$\begin{aligned} &\left[i\frac{\partial}{\partial t} + \frac{1}{2} i(R_e + R_a) \right. \\ &\left. - \sqrt{2} G_F \int dP' (1 - \cos\theta_\nu \cos\theta'_\nu)(\rho'_{ee} - \rho'_{xx}) \right] S \\ &= \sqrt{2} G_F (\rho_{xx} - \rho_{ee}) \int dP' (1 - \cos\theta_\nu \cos\theta'_\nu) S', \end{aligned} \tag{A2}$$

with $dP' = E'^2_\nu dE'_\nu d\cos\theta'_\nu d\phi'_\nu/(2\pi)^3$. In the linear stability analysis, we assume that the off-diagonal components are small enough to ignore the mode coupling with the diagonal components. Then, for the plane wave solution $S \propto Q \exp(-i\Omega t)$ in a homogeneous mode, we obtain

$$\begin{aligned} &[\Omega - (\Lambda_0 - \Lambda_1 \cos\theta_\nu) + i\Gamma] Q \\ &= -(a_0 - a_1 \cos\theta_\nu)(\rho_{ee} - \rho_{xx}), \end{aligned} \tag{A3}$$

where

$$\Gamma \equiv \frac{1}{2}[R_e(E_\nu) + R_a(E_\nu)], \tag{A4}$$

$$\Lambda_0 \equiv \sqrt{2} G_F \int dP (\rho_{ee} - \rho_{xx}), \tag{A5}$$

$$\Lambda_1 \equiv \sqrt{2} G_F \int dP \cos\theta_\nu (\rho_{ee} - \rho_{xx}), \tag{A6}$$

$$a_0 \equiv \sqrt{2} G_F \int dP Q, \tag{A7}$$

$$a_1 \equiv \sqrt{2} G_F \int dP \cos\theta_\nu Q. \tag{A8}$$

By solving Eq. (A3), we derive the eigenfunction Q as

$$Q = -\frac{(a_0 - a_1 \cos\theta_\nu)(\rho_{ee} - \rho_{xx})}{\Omega - (\Lambda_0 - \Lambda_1 \cos\theta_\nu) + i\Gamma}, \tag{A9}$$

and also describe a_0 and a_1 as

$$a_0 = -\sqrt{2} G_F \int dP \frac{(a_0 - a_1 \cos\theta_\nu)(\rho_{ee} - \rho_{xx})}{\Omega - (\Lambda_0 - \Lambda_1 \cos\theta_\nu) + i\Gamma}, \tag{A10}$$

$$a_1 = -\sqrt{2} G_F \int dP \cos\theta_\nu \frac{(a_0 - a_1 \cos\theta_\nu)(\rho_{ee} - \rho_{xx})}{\Omega - (\Lambda_0 - \Lambda_1 \cos\theta_\nu) + i\Gamma}. \tag{A11}$$

The matrix expression of the above two equations is

$$\begin{pmatrix} a_0 \\ a_1 \end{pmatrix} = \begin{pmatrix} -I_0 & I_1 \\ -I_1 & I_2 \end{pmatrix} \begin{pmatrix} a_0 \\ a_1 \end{pmatrix}, \tag{A12}$$

where

$$I_n = \sqrt{2} G_F \int dP \cos^n\theta_\nu \frac{(\rho_{ee} - \rho_{xx})}{\Omega - (\Lambda_0 - \Lambda_1 \cos\theta_\nu) + i\Gamma}, \tag{A13}$$

and the nontrivial solutions for a_0 and a_1 exist when the following condition is satisfied:

$$D(\Omega) \equiv (1 + I_0)(1 - I_2) + I_1^2 = 0. \tag{A14}$$

We derive a dispersion relation $\Omega \equiv \omega_p + i\gamma$ for the homogeneous mode as the solution of Eq. (A14). In Figs. 4, 5, 8, and 17, we plot $|D|$ on the $\omega_p - \gamma$ plane for the root finding. The values of $|D|$ are described by the color bar and the combinations of ω_p and γ, where $|D| \sim 0$ (blue regions), are the dispersion relations of the systems. The $\gamma > 0$ ($\gamma \leqq 0$) solutions correspond to growing (decaying) modes.

The origin of CFI modes is the collision rates Γ in the denominator of Eq. (A13). If we find the $\gamma > 0$ solutions, they are possible CFI modes. In the collisionless case, or $\Gamma = 0$, on the other hand, Eq. (A3) becomes the equation for the pure FFCs in the homogeneous case. By solving Eq. (A14) with $\Gamma = 0$, we can determine whether a system is stable or unstable for FFC modes. Moreover, the analysis

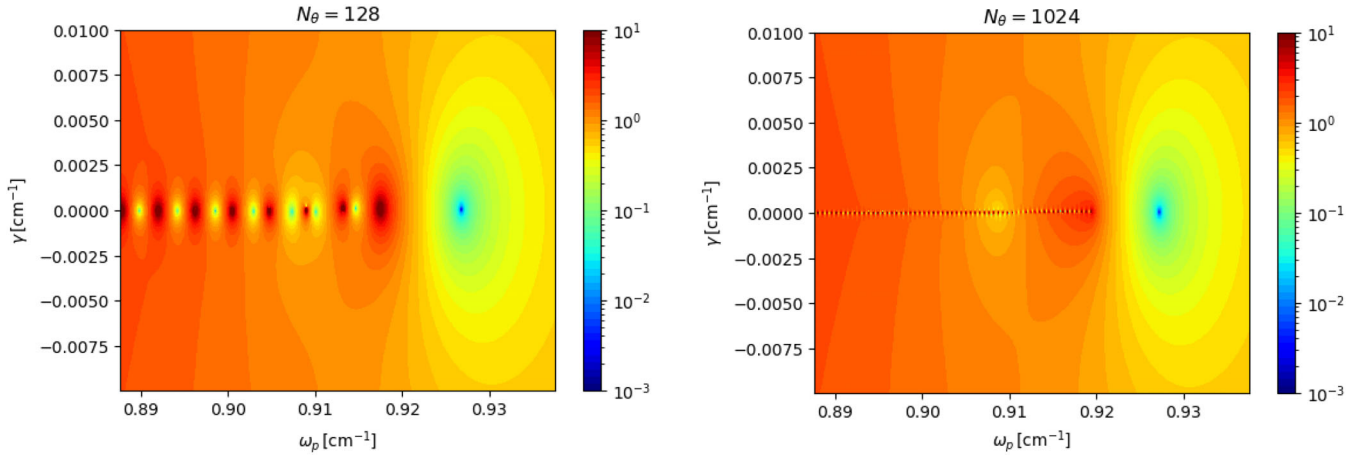

FIG. 17. Dispersion relation diagrams by the linear stability analysis at $t = 4 \times 10^{-6}$ s in the ST model. Left/right: the results of $N_{\theta_\nu} = 128$ and 1024, respectively.

of $\Gamma = 0$ tells us important information for CFI modes. Since Γ is always real, it changes not the real part of Ω (ω_p) but the imaginary part (γ). Hence, if the $\gamma > 0$ modes in the $\Gamma \neq 0$ analysis become stable ones in the $\Gamma = 0$ analysis at the same ω_p, we confirm that they are CFI modes.

It should be noted that we can see the presence of poles (or branch cuts) leading to spurious modes in the denominator in Eq. (A13) [79]. For $\Lambda_{0,1} > 0$, the branch cut spans from $\Lambda_0 - \Lambda_1$ to $\Lambda_0 + \Lambda_1$ on the axis of $\gamma = i\Gamma(E_\nu)$ and is replaced with spurious modes by discretizing the angular integration in Eq. (A13). For example, Fig. 17 shows the results of linear stability analysis for the ST model at $t = 4 \times 10^{-6}$ s. Left and right panels show the cases with $N_{\theta_\nu} = 128$ and 1024, respectively. Spurious modes appear at different positions in the dispersion relation diagram depending on angular resolution, whereas regardless of angular resolution, the actual solution appears in the same position. Following this strategy, we select the actual solution of the dispersion relations. For this example, the actual solution is found at $\omega_p \sim 0.925$.

[1] S. Samuel, Neutrino oscillations in dense neutrino gases, Phys. Rev. D **48**, 1462 (1993).
[2] G. Sigl and G. Raffelt, General kinetic description of relativistic mixed neutrinos, Nucl. Phys. **B406**, 423 (1993).
[3] G. Sigl, Neutrino mixing constraints and supernova nucleosynthesis, Phys. Rev. D **51**, 4035 (1995).
[4] R. F. Sawyer, Speed-up of neutrino transformations in a supernova environment, Phys. Rev. D **72**, 045003 (2005).
[5] L. Johns, Collisional Flavor Instabilities of Supernova Neutrinos, Phys. Rev. Lett. **130**, 191001 (2023).
[6] O. Just, S. Abbar, M.-R. Wu, I. Tamborra, H.-T. Janka, and F. Capozzi, Fast neutrino conversion in hydrodynamic simulations of neutrino-cooled accretion disks, Phys. Rev. D **105**, 083024 (2022).
[7] R. Fernández, S. Richers, N. Mulyk, and S. Fahlman, Fast flavor instability in hypermassive neutron star disk outflows, Phys. Rev. D **106**, 103003 (2022).
[8] Z. Xiong, M.-R. Wu, G. Martínez-Pinedo, T. Fischer, M. George, C.-Y. Lin, and L. Johns, Evolution of collisional neutrino flavor instabilities in spherically symmetric supernova models, Phys. Rev. D **107**, 083016 (2023).
[9] H. Nagakura, Roles of Fast Neutrino-Flavor Conversion on the Neutrino-Heating Mechanism of Core-Collapse Supernova, Phys. Rev. Lett. **130**, 211401 (2023).
[10] J. Ehring, S. Abbar, H.-T. Janka, and G. Raffelt, Fast neutrino flavor conversion in core-collapse supernovae: A parametric study in 1D models, Phys. Rev. D **107**, 103034 (2023).
[11] T. Morinaga, Fast neutrino flavor instability and neutrino flavor lepton number crossings, Phys. Rev. D **105**, L101301 (2022).
[12] B. Dasgupta, Collective Neutrino Flavor Instability Requires a Crossing, Phys. Rev. Lett. **128**, 081102 (2022).
[13] H. Nagakura and M. Zaizen, Time-Dependent and Quasi-steady Features of Fast Neutrino-Flavor Conversion, Phys. Rev. Lett. **129**, 261101 (2022).
[14] M. Zaizen and H. Nagakura, Simple method for determining asymptotic states of fast neutrino-flavor conversion, Phys. Rev. D **107**, 103022 (2023).
[15] B. Dasgupta, A. Mirizzi, and M. Sen, Fast neutrino flavor conversions near the supernova core with realistic flavor-dependent angular distributions, J. Cosmol. Astropart. Phys. 02 (2017) 019.

[16] I. Tamborra, L. Hüdepohl, G. G. Raffelt, and H.-T. Janka, Flavor-dependent neutrino angular distribution in core-collapse supernovae, Astrophys. J. **839**, 132 (2017).
[17] B. Dasgupta, A. Mirizzi, and M. Sen, Simple method of diagnosing fast flavor conversions of supernova neutrinos, Phys. Rev. D **98**, 103001 (2018).
[18] S. Abbar, H. Duan, K. Sumiyoshi, T. Takiwaki, and M. C. Volpe, On the occurrence of fast neutrino flavor conversions in multidimensional supernova models, Phys. Rev. D **100**, 043004 (2019).
[19] H. Nagakura, T. Morinaga, C. Kato, and S. Yamada, Fast-pairwise collective neutrino oscillations associated with asymmetric neutrino emissions in core-collapse supernovae, Astrophys. J. **886**, 139 (2019).
[20] M. Delfan Azari, S. Yamada, T. Morinaga, W. Iwakami, H. Okawa, H. Nagakura, and K. Sumiyoshi, Linear analysis of fast-pairwise collective neutrino oscillations in core-collapse supernovae based on the results of Boltzmann simulations, Phys. Rev. D **99**, 103011 (2019).
[21] M. Delfan Azari, S. Yamada, T. Morinaga, H. Nagakura, S. Furusawa, A. Harada, H. Okawa, W. Iwakami, and K. Sumiyoshi, Fast collective neutrino oscillations inside the neutrino sphere in core-collapse supernovae, Phys. Rev. D **101**, 023018 (2020).
[22] T. Morinaga, H. Nagakura, C. Kato, and S. Yamada, Fast neutrino-flavor conversion in the preshock region of core-collapse supernovae, Phys. Rev. Res. **2**, 012046 (2020).
[23] S. Abbar, H. Duan, K. Sumiyoshi, T. Takiwaki, and M. C. Volpe, Fast neutrino flavor conversion modes in multidimensional core-collapse supernova models: The role of the asymmetric neutrino distributions, Phys. Rev. D **101**, 043016 (2020).
[24] S. Abbar, Searching for fast neutrino flavor conversion modes in core-collapse supernova simulations, J. Cosmol. Astropart. Phys. 05 (2020) 027.
[25] R. Glas, H.-T. Janka, F. Capozzi, M. Sen, B. Dasgupta, A. Mirizzi, and G. Sigl, Fast neutrino flavor instability in the neutron-star convection layer of three-dimensional supernova models, Phys. Rev. D **101**, 063001 (2020).
[26] F. Capozzi, M. Chakraborty, S. Chakraborty, and M. Sen, Mu-Tau Neutrinos: Influencing Fast Flavor Conversions in Supernovae, Phys. Rev. Lett. **125**, 251801 (2020).
[27] S. Abbar, F. Capozzi, R. Glas, H.-T. Janka, and I. Tamborra, On the characteristics of fast neutrino flavor instabilities in three-dimensional core-collapse supernova models, Phys. Rev. D **103**, 063033 (2021).
[28] F. Capozzi, S. Abbar, R. Bollig, and H. T. Janka, Fast neutrino flavor conversions in one-dimensional core-collapse supernova models with and without muon creation, Phys. Rev. D **103**, 063013 (2021).
[29] H. Nagakura, A. Burrows, L. Johns, and G. M. Fuller, Where, when, and why: Occurrence of fast-pairwise collective neutrino oscillation in three-dimensional core-collapse supernova models, Phys. Rev. D **104**, 083025 (2021).
[30] A. Harada and H. Nagakura, Prospects of fast flavor neutrino conversion in rotating core-collapse supernovae, Astrophys. J. **924**, 109 (2022).
[31] R. Akaho, A. Harada, H. Nagakura, W. Iwakami, H. Okawa, S. Furusawa, H. Matsufuru, K. Sumiyoshi, and S. Yamada, Protoneutron star convection simulated with a new general relativistic Boltzmann neutrino radiation-hydrodynamics code, Astrophys. J. **944**, 60 (2023).
[32] M.-R. Wu and I. Tamborra, Fast neutrino conversions: Ubiquitous in compact binary merger remnants, Phys. Rev. D **95**, 103007 (2017).
[33] M.-R. Wu, I. Tamborra, O. Just, and H.-T. Janka, Imprints of neutrino-pair flavor conversions on nucleosynthesis in ejecta from neutron-star merger remnants, Phys. Rev. D **96**, 123015 (2017).
[34] M. George, M.-R. Wu, I. Tamborra, R. Ardevol-Pulpillo, and H.-T. Janka, Fast neutrino flavor conversion, ejecta properties, and nucleosynthesis in newly-formed hypermassive remnants of neutron-star mergers, Phys. Rev. D **102**, 103015 (2020).
[35] X. Li and D. M. Siegel, Neutrino Fast Flavor Conversions in Neutron-Star Postmerger Accretion Disks, Phys. Rev. Lett. **126**, 251101 (2021).
[36] S. Richers, Evaluating approximate flavor instability metrics in neutron star mergers, Phys. Rev. D **106**, 083005 (2022).
[37] E. Grohs, S. Richers, S. M. Couch, F. Foucart, J. P. Kneller, and G. C. McLaughlin, Neutrino fast flavor instability in three dimensions for a neutron star merger, arXiv:2207.02214.
[38] S. Abbar and M. C. Volpe, On fast neutrino flavor conversion modes in the nonlinear regime, Phys. Lett. B **790**, 545 (2019).
[39] S. Bhattacharyya and B. Dasgupta, Fast Flavor Depolarization of Supernova Neutrinos, Phys. Rev. Lett. **126**, 061302 (2021).
[40] J. D. Martin, C. Yi, and H. Duan, Dynamic fast flavor oscillation waves in dense neutrino gases, Phys. Lett. B **800**, 135088 (2020).
[41] S. Richers, D. E. Willcox, N. M. Ford, and A. Myers, Particle-in-cell simulation of the neutrino fast flavor instability, Phys. Rev. D **103**, 083013 (2021).
[42] S. Richers, D. Willcox, and N. Ford, Neutrino fast flavor instability in three dimensions, Phys. Rev. D **104**, 103023 (2021).
[43] M.-R. Wu, M. George, C.-Y. Lin, and Z. Xiong, Collective fast neutrino flavor conversions in a 1D box: Initial conditions and long-term evolution, Phys. Rev. D **104**, 103003 (2021).
[44] M. Zaizen and T. Morinaga, Nonlinear evolution of fast neutrino flavor conversion in the preshock region of core-collapse supernovae, Phys. Rev. D **104**, 083035 (2021).
[45] S. Abbar and F. Capozzi, Suppression of fast neutrino flavor conversions occurring at large distances in core-collapse supernovae, J. Cosmol. Astropart. Phys. 03 (2022) 051.
[46] S. Richers, H. Duan, M.-R. Wu, S. Bhattacharyya, M. Zaizen, M. George, C.-Y. Lin, and Z. Xiong, Code comparison for fast flavor instability simulations, Phys. Rev. D **106**, 043011 (2022).
[47] S. Bhattacharyya and B. Dasgupta, Elaborating the ultimate fate of fast collective neutrino flavor oscillations, Phys. Rev. D **106**, 103039 (2022).
[48] L. Johns, H. Nagakura, G. M. Fuller, and A. Burrows, Neutrino oscillations in supernovae: Angular moments and fast instabilities, Phys. Rev. D **101**, 043009 (2020).

[49] I. Padilla-Gay, I. Tamborra, and G. G. Raffelt, Neutrino Flavor Pendulum Reloaded: The Case of Fast Pairwise Conversion, Phys. Rev. Lett. **128**, 121102 (2022).
[50] H. Sasaki and T. Takiwaki, A detailed analysis of the dynamics of fast neutrino flavor conversions with scattering effects, Prog. Theor. Exp. Phys. **2022**, 073E01 (2022).
[51] I. Padilla-Gay, I. Tamborra, and G. G. Raffelt, Neutrino fast flavor pendulum. II. Collisional damping, Phys. Rev. D **106**, 103031 (2022).
[52] F. Capozzi, B. Dasgupta, A. Mirizzi, M. Sen, and G. Sigl, Collisional Triggering of Fast Flavor Conversions of Supernova Neutrinos, Phys. Rev. Lett. **122**, 091101 (2019).
[53] S. A. Richers, G. C. McLaughlin, J. P. Kneller, and A. Vlasenko, Neutrino quantum kinetics in compact objects, Phys. Rev. D **99**, 123014 (2019).
[54] J. D. Martin, J. Carlson, V. Cirigliano, and H. Duan, Fast flavor oscillations in dense neutrino media with collisions, Phys. Rev. D **103**, 063001 (2021).
[55] S. Shalgar and I. Tamborra, Change of direction in pairwise neutrino conversion physics: The effect of collisions, Phys. Rev. D **103**, 063002 (2021).
[56] C. Kato and H. Nagakura, Effects of energy-dependent scatterings on fast neutrino flavor conversions, Phys. Rev. D **106**, 123013 (2022).
[57] R. S. L. Hansen, S. Shalgar, and I. Tamborra, Enhancement or damping of fast neutrino flavor conversions due to collisions, Phys. Rev. D **105**, 123003 (2022).
[58] G. Sigl, Simulations of fast neutrino flavor conversions with interactions in inhomogeneous media, Phys. Rev. D **105**, 043005 (2022).
[59] S. Shalgar and I. Tamborra, Supernova neutrino decoupling is altered by flavor conversion, arXiv:2206.00676.
[60] S. Shalgar and I. Tamborra, Neutrino flavor conversion, advection, and collisions: The full solution, Phys. Rev. D **107**, 063025 (2023).
[61] H. Nagakura and M. Zaizen, Connecting small-scale to large-scale structures of fast neutrino-flavor conversion, Phys. Rev. D **107**, 063033 (2023).
[62] I. Tamborra and S. Shalgar, New developments in flavor evolution of a dense neutrino gas, Annu. Rev. Nucl. Part. Sci. **71**, 165 (2021).
[63] F. Capozzi and N. Saviano, Neutrino flavor conversions in high-density astrophysical and cosmological environments, Universe **8**, 94 (2022).
[64] S. Richers and M. Sen, Fast flavor transformations, arXiv:2207.03561.
[65] Y.-C. Lin and H. Duan, Collision-induced flavor instability in dense neutrino gases with energy-dependent scattering, Phys. Rev. D **107**, 083034 (2023).
[66] J. Liu, M. Zaizen, and S. Yamada, A systematic study on the resonance in collisional neutrino flavor instability, arXiv:2302.06263.
[67] L. Johns and Z. Xiong, Collisional instabilities of neutrinos and their interplay with fast flavor conversion in compact objects, Phys. Rev. D **106**, 103029 (2022).
[68] Z. Xiong, L. Johns, M.-R. Wu, and H. Duan, Collisional flavor instability in dense neutrino gases, arXiv:2212.03750.
[69] C. Volpe, Neutrino quantum kinetic equations, Int. J. Mod. Phys. E **24**, 1541009 (2015).
[70] R. Bollig, H. T. Janka, A. Lohs, G. Martínez- Pinedo, C. J. Horowitz, and T. Melson, Muon Creation in Supernova Matter Facilitates Neutrino-Driven Explosions, Phys. Rev. Lett. **119**, 242702 (2017).
[71] K. Sumiyoshi and S. Yamada, Neutrino transfer in three dimensions for core-collapse supernovae. I. Static configurations, Astrophys. J. Suppl. Ser. **199**, 17 (2012).
[72] C. Kato, H. Nagakura, Y. Hori, and S. Yamada, Neutrino transport with Monte Carlo method. I. Toward fully consistent implementation of nucleon recoils in core-collapse supernova simulations, Astrophys. J. **897**, 43 (2020).
[73] H. Duan, G. M. Fuller, J. Carlson, and Y.-Z. Qian, Simulation of coherent nonlinear neutrino flavor transformation in the supernova environment: Correlated neutrino trajectories, Phys. Rev. D **74**, 105014 (2006).
[74] S. Hannestad, G. G. Raffelt, G. Sigl, and Y. Y. Y. Wong, Self-induced conversion in dense neutrino gases: Pendulum in flavor space, Phys. Rev. D **74**, 105010 (2006).
[75] S. Sarikas, D. de Sousa Seixas, and G. Raffelt, Spurious instabilities in multiangle simulations of collective flavor conversion, Phys. Rev. D **86**, 125020 (2012).
[76] S. Bhattacharyya and B. Dasgupta, Late-time behavior of fast neutrino oscillations, Phys. Rev. D **102**, 063018 (2020).
[77] S. Shalgar and I. Tamborra, Symmetry breaking induced by pairwise conversion of neutrinos in compact sources, Phys. Rev. D **105**, 043018 (2022).
[78] L. Johns and H. Nagakura, Self-consistency in models of neutrino scattering and fast flavor conversion, Phys. Rev. D **106**, 043031 (2022).
[79] T. Morinaga and S. Yamada, Linear stability analysis of collective neutrino oscillations without spurious modes, Phys. Rev. D **97**, 023024 (2018).